

1

*Electronic Supplementary Information*

2 **An Interface Stabilized Perovskite Solar Cell with High Stabilized Efficiency**  
3 **and Low Voltage Loss**

4 **Authors:** Jason J. Yoo,<sup>a</sup> Sarah Wieghold,<sup>b</sup> Melany C. Sponseller,<sup>c</sup> Matthew R. Chua,<sup>c</sup> Sophie N.  
5 Bertram,<sup>a</sup> Noor Titan Putri Hartono,<sup>b</sup> Jason S. Tresback,<sup>d</sup> Eric C. Hansen,<sup>a</sup> Juan-Pablo Correa-  
6 Baena,<sup>b</sup> Vladimir Bulović,<sup>c</sup> Tonio Buonassisi,<sup>b</sup> Seong Sik Shin,<sup>b,e\*</sup> Moungi G. Bawendi<sup>a\*</sup>.

7 **Affiliations:**

8 <sup>a</sup>Department of Chemistry, Massachusetts Institute of Technology, 77 Massachusetts Avenue,  
9 Cambridge, Massachusetts 02139, USA.

10 <sup>b</sup>Department of Mechanical Engineering, Massachusetts Institute of Technology, 77  
11 Massachusetts Avenue, Cambridge, Massachusetts 02139, USA

12 <sup>c</sup>Department of Electrical Engineering and Computer Science, Massachusetts Institute of  
13 Technology, 77 Massachusetts Avenue, Cambridge, Massachusetts 02139, USA

14 <sup>d</sup>Center for Nanoscale Systems, Harvard University, Cambridge, Massachusetts 02138, USA.

15 <sup>e</sup>Division of Advanced Materials, Korea Research Institute of Chemical Technology, 141  
16 Gajeong-Ro, Yuseong-Gu, Daejeon 34114, Korea.

17

18 \*Correspondence authors. Email: mgb@mit.edu (M.G.B); sss85@kRICT.re.kr (S.S.S)

19

20 **Methods**

21 **Chemicals**

22 Fluorine-doped tin oxide (FTO) were purchased from Pilkington (TEC8). Titanium diisopropoxide  
23 bis(acetylacetone) solution (75 wt. % in isopropanol), DMF, DMSO, diethyl ether,  
24 chlorobenzene, chloroform, isopropyl alcohol, Lithium Bis(trifluoromethanesulfonyl)imide salt  
25 (Li-TFSI), and 4-*tert*-butylpyridine (tBP) were purchased from Sigma-Aldrich. TiO<sub>2</sub> paste (SC-  
26 HT040) was purchased from ShareChem. 2,2',7,7'-Tetrakis(N,N -di-p -methoxyphenylamino)-  
27 9,9'-spirobifluorene (Spiro-OMeTAD, LT-S922) and Tris(2-(1H -pyrazol-1-yl)-4-*tert*-  
28 butylpyridine)-cobalt(III)Tris(bis(trifluoromethylsulfonyl)imide)) salt (Co(III) TFSI) were  
29 purchased from Lumtec. Methylammonium chloride (MACl) was purchased from Dyenamo.  
30 Formamidinium iodide (FAI), methylammonium bromide (MABr), n-butylammonium bromide  
31 (C<sub>4</sub>Br), n-hexylammonium bromide (C<sub>6</sub>Br), and n-octylammonium bromide (C<sub>8</sub>Br) were  
32 purchased from GreatCell Solar. Lead iodide (PbI<sub>2</sub>) and lead bromide (PbBr<sub>2</sub>) were purchased  
33 from TCI America. Au pellets were purchased from Kurt J. Lesker.

34

35 **Device fabrication**

36 FTO substrates were cleaned by sonicating in deionized water, acetone, and isopropyl alcohol for  
37 10 min each. A blocking TiO<sub>2</sub> layer was deposited via spray pyrolysis using a 20 mM titanium  
38 diisopropoxide bis(acetylacetone) solution at 450 °C. A mesoporous TiO<sub>2</sub> layer was deposited  
39 by spin coating a TiO<sub>2</sub> paste and was sintered at 500 °C for 2 hrs. A Li-TFSI solution (45 mg/mL  
40 in acetonitrile) was spin coated onto the TiO<sub>2</sub> layer and heat treated at 500 °C for 2 hrs. The  
41 FTO/TiO<sub>2</sub> substrate was plasma treated to make the surface hydrophilic before pumping it into a  
42 nitrogen glovebox. The (FAPbI<sub>3</sub>)<sub>0.92</sub>(MAPbBr<sub>3</sub>)<sub>0.08</sub> perovskite solution (1.53 M PbI<sub>2</sub>, 1.4 M FAI,

43 0.11 M MAPbBr<sub>3</sub>, 0.5 M MACl in DMF:DMSO=8:1 volume ratio) was spin coated at 1000 rpm  
44 for 10 sec and 5000 rpm for 30 sec onto the FTO/TiO<sub>2</sub> substrate. 10 seconds into the 5000 rpm  
45 setting, 600 μL of diethyl ether was deposited and the FTO/TiO<sub>2</sub>/perovskite sample was heat  
46 treated at 150 °C for 10 min. For *in-situ* LP synthesis, a solution of LP precursors (10 mM in  
47 chloroform or IPA) was deposited and spin coated at 5000 rpm for 30 sec on the  
48 FTO/TiO<sub>2</sub>/perovskite sample, followed by heat treatment at 100 °C for 5 min (Note: our  
49 additional solubility testing showed that LP precursors are not soluble in chlorobenzene, 1,2-  
50 dichlorobenzene, and toluene). The hole transporting layer (HTL) was deposited by preparing the  
51 HTL solution consisting of 50 mg of Spiro-OMeTAD, 19.5 μL of tBP, 5 μL of Co(III) TFSI  
52 solution (0.25 M in acetonitrile), 11.5 μL of Li-TFSI solution (1.8 M in acetonitrile), and 547 μL  
53 of chlorobenzene. 70 μL of the HTL solution is loaded onto the perovskite substrate and spin  
54 coated at 4000 rpm for 20 sec with the ramp of 2000 rpm/sec. The HTL solution preparation and  
55 deposition is performed inside a nitrogen glovebox. The Au electrode (100 nm) was deposited by  
56 thermal evaporation.

57

## 58 **Device Characterization**

59 Current density-voltage (*J-V*) curves were recorded using a solar simulator (Newport,  
60 Oriel Class A, 91195A) and a source meter (Keithley 2420). The illumination was set to AM  
61 1.5G and calibrated to 100 mW/cm<sup>2</sup> using a calibrated silicon reference cell. The step voltage is  
62 10 mV and the delay time is 50 ms. The active area was controlled by using a dark mask with an  
63 aperture of 0.095 cm<sup>2</sup> (used at both Newport and at MIT). For the stability measurement, the  
64 devices were encapsulated and tested under AM 1.5G and 100 mW/cm<sup>2</sup> in an ambient condition.

65 The MPP was measured via perturb and observe algorithm implemented onto a custom LabView  
66 code.

67

## 68 **Scanning Electron Microscope (SEM) and X-ray Diffraction (XRD)**

69 The SEM images were recorded using a Zeiss Merlin High-resolution SEM and the XRD  
70 patterns were collected using a Rigaku SmartLab and a Bruker D8 Discovery Diffractometer  
71 with a General Area Detector Diffraction System.

72

## 73 **AFM and KPFM**

74 AFM measurements were performed with a Cypher S (Asylum Research). Topography  
75 images were collected using an uncoated silicon tip at a resonant frequency of 300 kHz and a  
76 spring constant of 26 N/m in tapping mode. All images are shown with line-wise flattening to  
77 remove tilting effects of the substrate plane. Root mean square (RMS) values were determined  
78 by 20 x 20  $\mu\text{m}^2$  images. Kelvin probe force measurements were performed with a MFP-3D AFM  
79 (Asylum Research) in air. PtIr and electilevers were employed at a lift height of 25 nm and with  
80 a 3 V AC bias applied to the tip to induce an electrostatic force between the tip and sample. The  
81 surface potential difference between the tip and sample is regarded as the DC bias applied to the  
82 tip in order to null the tip oscillations.

83

## 84 **Ultraviolet Photoelectron Spectroscopy (UPS)**

85 UPS was conducted in an Omicron ultrahigh vacuum (UHV) system with base pressure  
86 of approximately 1e-10 mbar. Perovskite films prepared on un-patterned ITO-coated glass were  
87 grounded to steel UPS sample plates via carbon tape and subsequently loaded from air into the

88 UHV system. Measurements were carried out at a pressure of approximately 1e-7 mbar and  
89 sample bias of -5.0V, under excitation from the He I line (21.22eV) of a helium discharge lamp.  
90 Spectra were collected using a constant analyzer energy of 5eV, step size of 20 meV, and step  
91 delay of 20ms and were calibrated to the Fermi edge of a thermally-evaporated Au sample.  
92 Cutoff energies were found by intersecting a linear fit of each cutoff region with a linear  
93 extrapolation of the corresponding baseline.

94

### 95 **Time Resolved Photoluminescence (TRPL)**

96 Photoluminescence lifetimes were collected using a 532 nm picosecond pulsed diode  
97 laser (Picoquant; LDH-P-FA-266) adjusted to a repetition rate of 200kHz using a pulse generator  
98 (Stanford Research; DG535). The laser was set to an average power of 0.2 $\mu$ W using neutral  
99 density filters and focused to a 150  $\mu$ m spot on the perovskite film. The emission from the film  
100 was collected and collimated using an off-axis parabolic mirror (Thorlabs; MPD269V) and  
101 measured with a silicon single-photon avalanche diode (SPAD) detector (Micro Photon Devices;  
102 \$PD-100-C0C). Scattered laser excitation was suppressed using a 532 nm notch filter (Chroma;  
103 ZET532NF) and a 550 nm longpass filter (Thorlabs; FELH0550). The 532 nm laser harmonic  
104 was suppressed using a 900 nm shortpass filter (Thorlabs; FESH0900). Photon arrival times were  
105 recorded using a time-correlated single photon counting card (Picoquant; PicoHarp 300) and all  
106 analysis was performed in Matlab.

107

### 108 **Electroluminescence (EL) efficiency measurements**

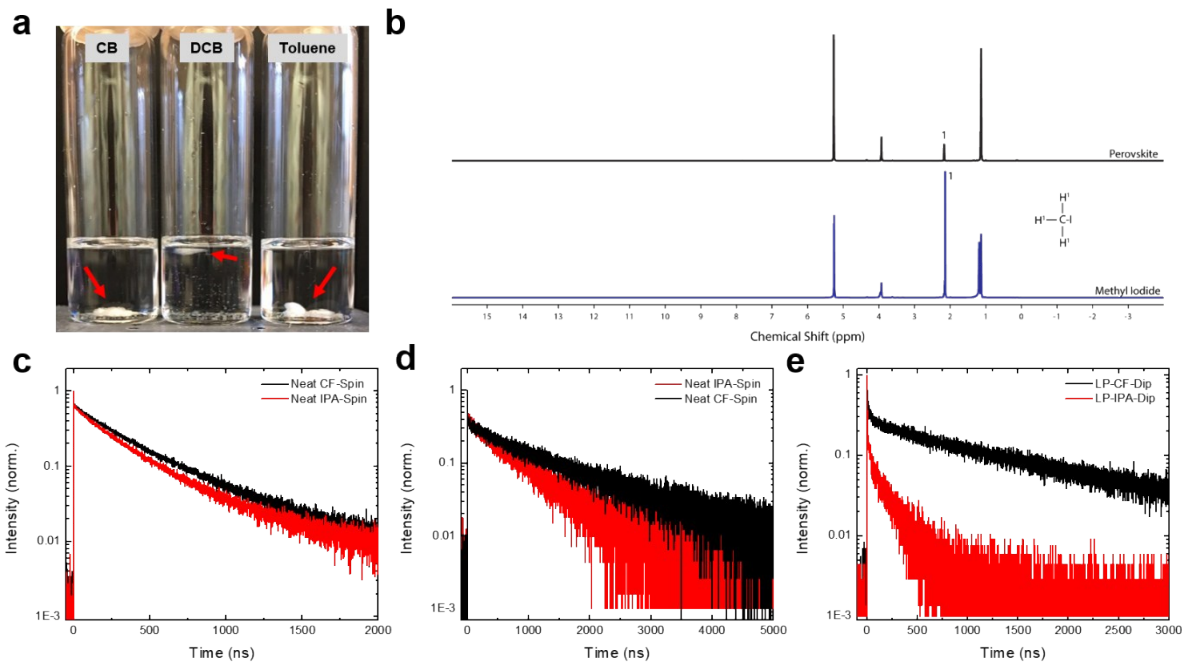
109 EL efficiency is measured in a nitrogen filled glovebox under ambient conditions in the  
110 dark. The device is voltage driven, and current is measured simultaneously by a Keithley 2636A

111 sourcemeter. Photocurrent is collected using a calibrated Newport 818-UV/DB Silicon  
112 photodetector coupled to a Newport 1835-C Multifunction Optical meter. EL spectra are  
113 collected using an Ocean Optics USB 2000 spectrometer using a multimode fiber positioned  
114 over the center of the active area.

115 As the device area (~0.32cm<sup>2</sup>) is comparable to the photodetector active area, the  
116 photodetector surface is positioned such that the active area is 17.0 mm from the top surface of  
117 the device. To prevent collection of waveguided emission, a black plastic baffle surrounds the  
118 edge of the device. We measured the emission profile to be approximately Lambertian (Extended  
119 Data Figure 9) and applied an appropriate multiplicative geometric factor to the photocurrent  
120 value collected.

121 EQE and radiance values are then obtained by scaling the corrected photocurrent values  
122 with the photodetector responsivity and EL spectrum. Note that the detector responsivity is  
123 relatively flat in the emission region and the observed variation in the EL spectra will account for  
124 a negligibly small variation in EQE. Current density and radiance values are calculated assuming  
125 the device active area is equal to the gold top contact area. It is found that a sweep rate below  
126 20mV/s is required for the EL to stabilize. The I-V-Photocurrent sweep is run by a custom  
127 Labview code.

128

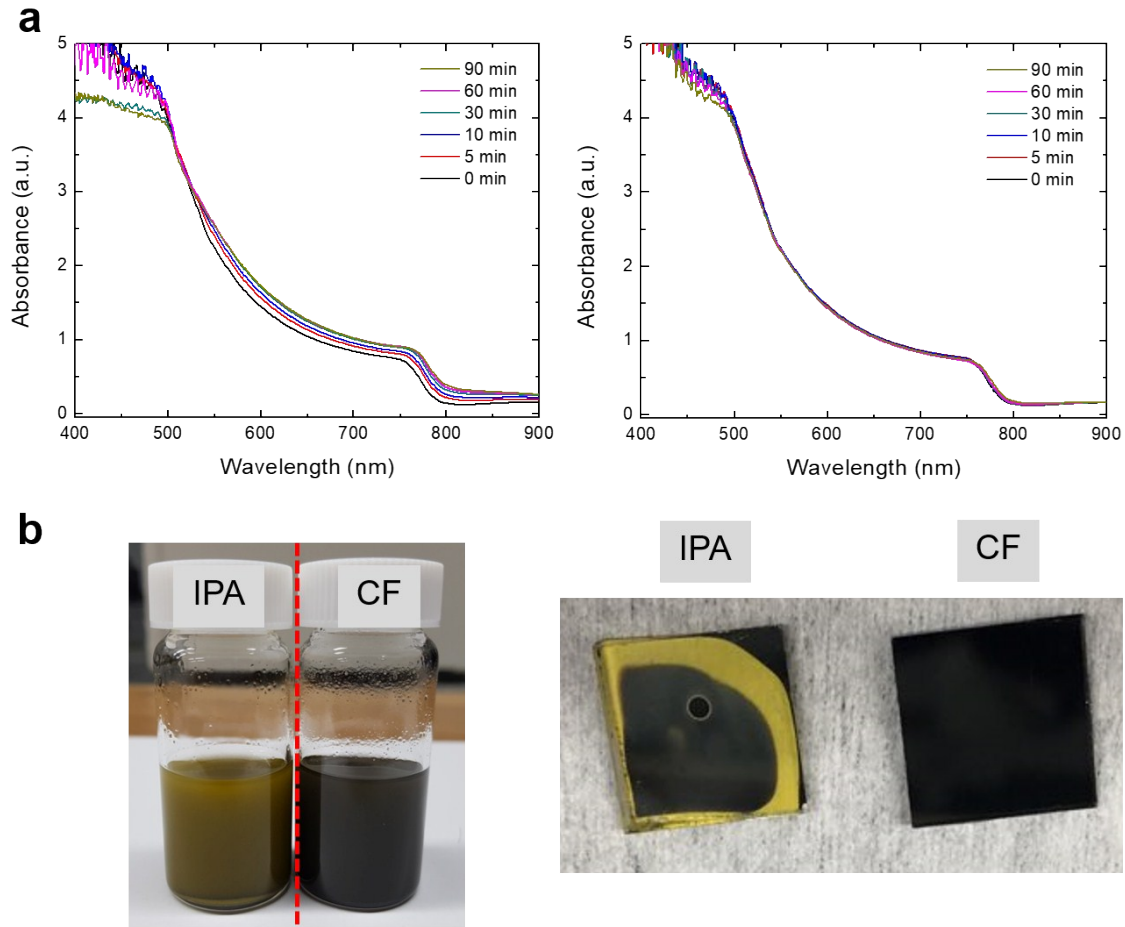


129

130 **Fig. S1 a**, Photograph of vials containing the LP precursor C<sub>6</sub>Br in chlorobenzene (CB), 1,2-  
 131 dichlorobenzene (DCB), and toluene. The precursor concentration is 2.5 mg/mL. The red arrows  
 132 points to insoluble precursor powder. **b**, <sup>1</sup>H NMR of 3D perovskite dipped in deuterated IPA and  
 133 methyl iodide in deuterated IPA. When the 3D perovskite is exposed to IPA, the  
 134 methylammonium iodide decomposes to methyl iodide and ammonia. The methyl iodide peak is  
 135 visible at ~2.1 ppm in perovskite sample. The peak at ~5.2 ppm is water and peaks at ~3.8 and  
 136 ~1.1 ppm is IPA peak. **c-e**, Lifetime traces of perovskite substrate fabricated inside the glovebox  
 137 with treatment with neat IPA and CF (**c**), fabricated in ambient condition with treatment with  
 138 neat IPA and CF (**d**) and LP precursor containing IPA and CF (**e**).

139

140

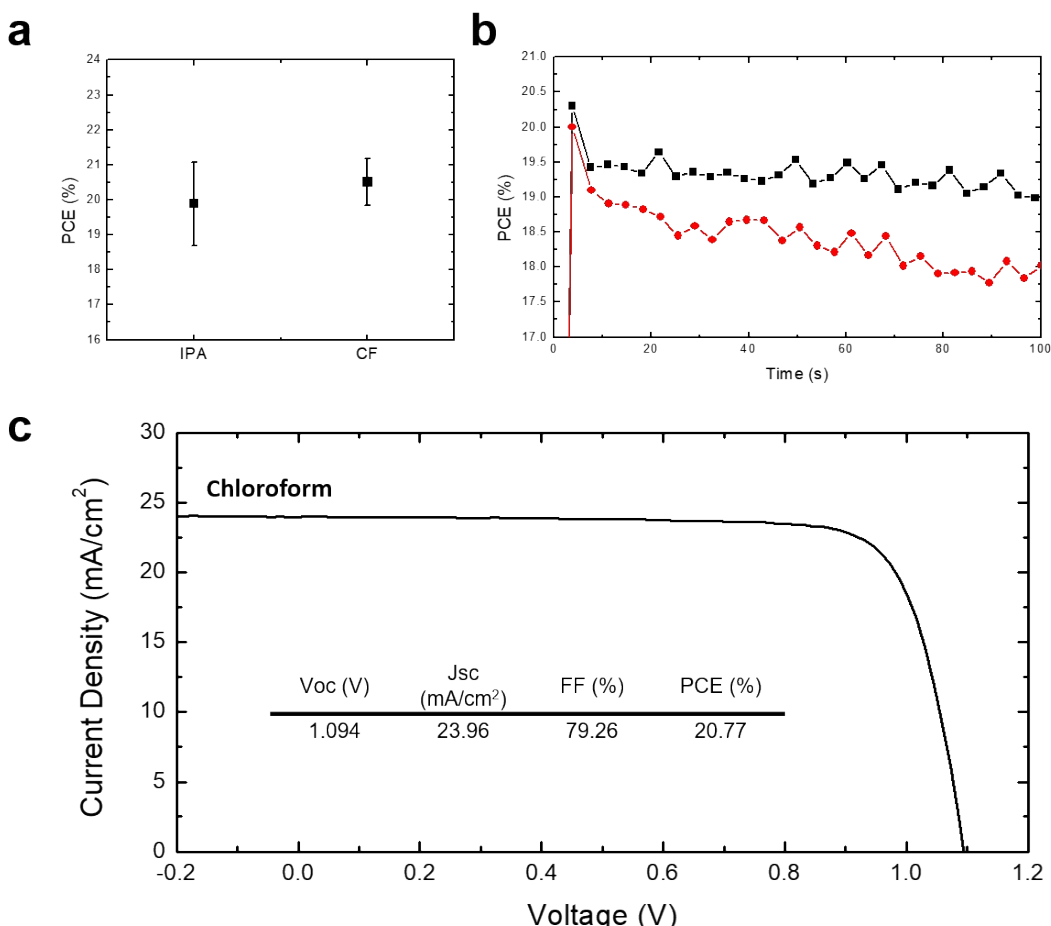


141

142 **Fig S2 a**, UVVis of 3D perovskite dipped in IPA (left) and CF (right). The UVVis of perovskite  
 143 substrate dipped in IPA shows higher scattering background due to roughening of the surface and  
 144 reduced relative absorbance in the ~500 nm region due to perovskite bleaching or destabilized  
 145 crystal phase. However, no change in optical response for CF is observed. The experiment was  
 146 carried in air. **b**, Photograph of perovskite powder (left) and thin film (right) exposed to IPA or  
 147 CF in air overnight. IPA causes perovskite bleaching whereas CF does not affect the perovskite  
 148 samples.

149

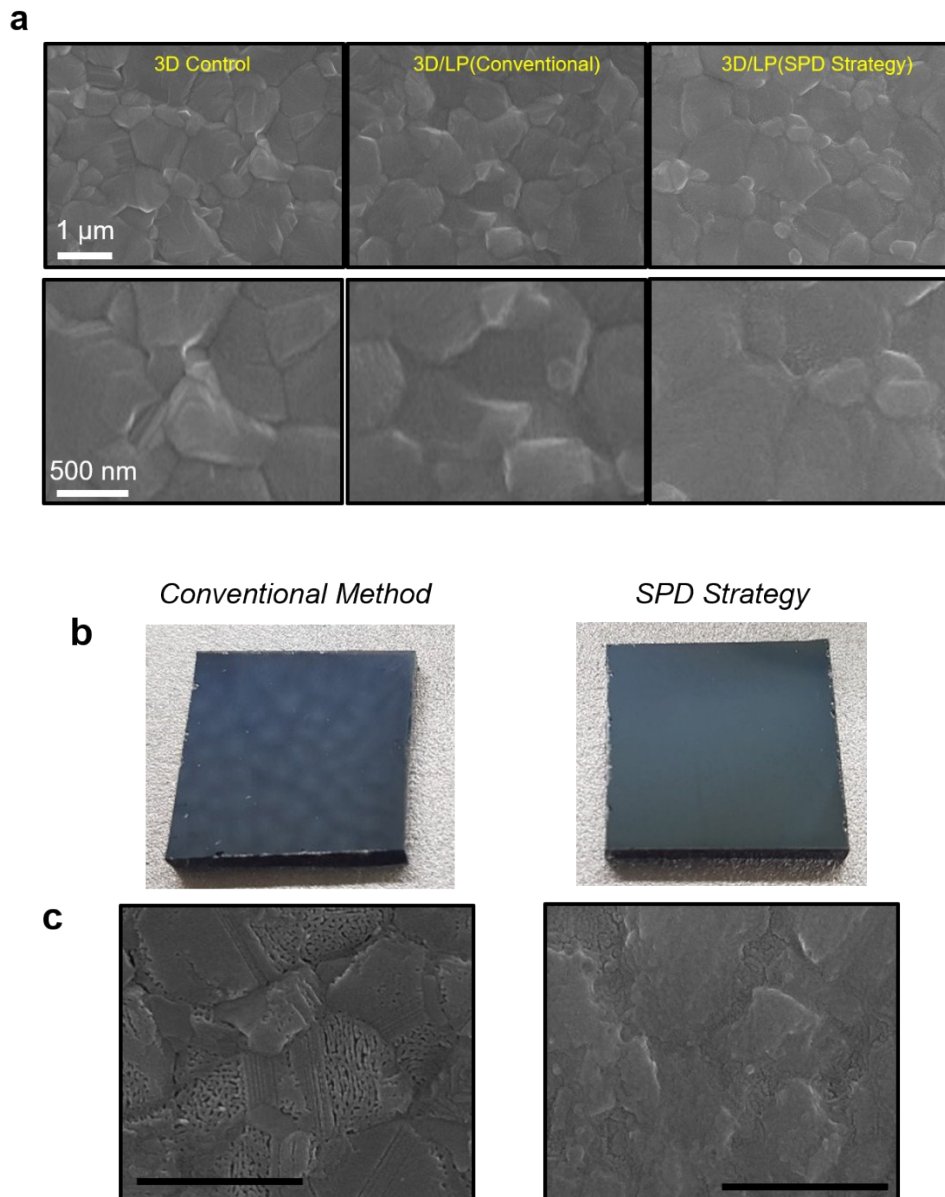
150



151

152 **Fig S3 a,b**, PCE (a) and MPP (b) on PSC fabricated with neat IPA or CF treatment. The neat  
 153 IPA (red trace) treated PSC results in lower efficiency and faster degradation under MPP  
 154 condition. **c**, *J-V* curve and device performance of PSC fabricated by soaking in CF overnight in  
 155 air prior to hole transport layer and Au deposition.

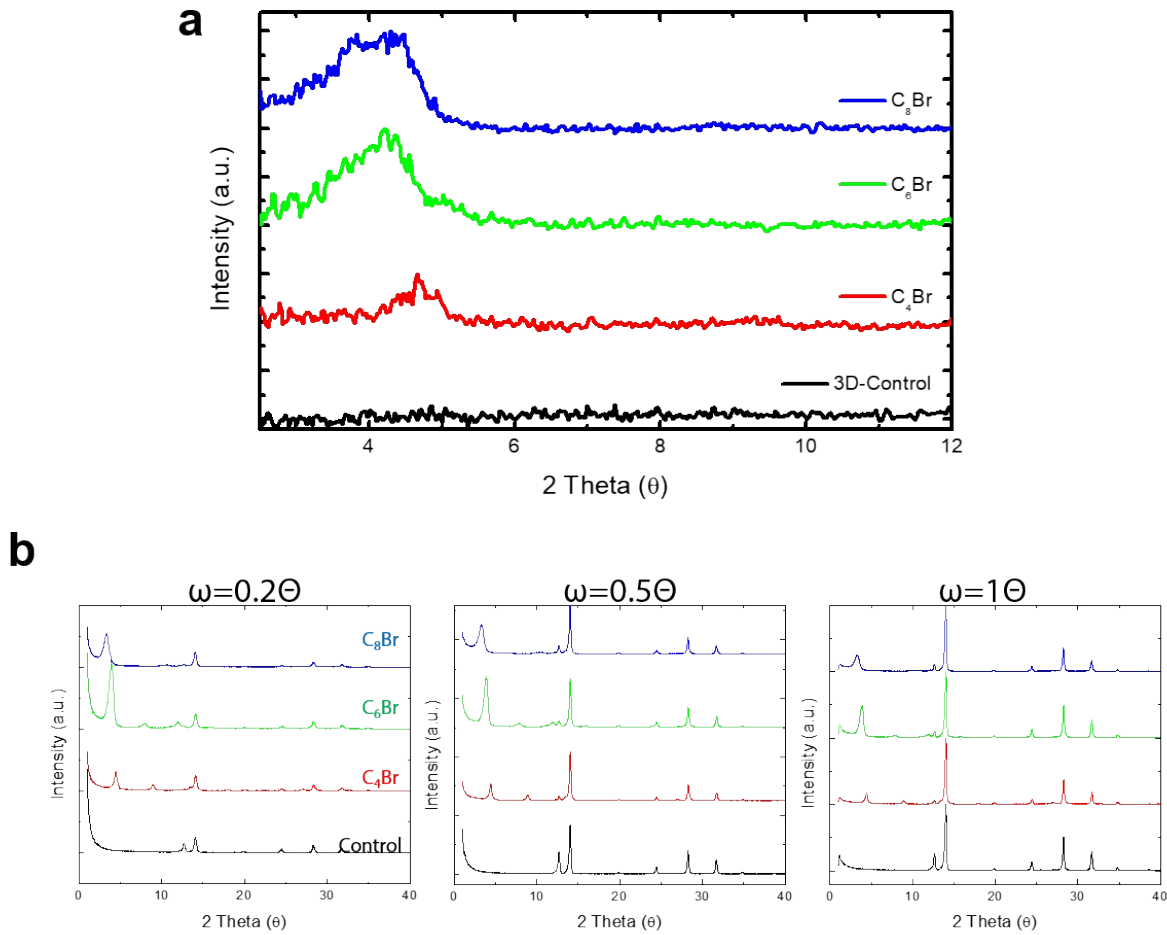
156



159 **Fig S4 a**, Planar SEM images of 3D, 3D/LP (IPA), and 3D/LP (CF) perovskites where C<sub>6</sub>Br was  
 160 used for the LP. The grain boundary is most distinct for the 3D perovskite and least distinct for  
 161 3D/LP (CF) perovskite. **b,c**, Photograph (**b**) and SEM image (**c**) of 3D/LP substrates fabricated  
 162 using conventional method or SPD strategy with long solution exposure time by loading the  
 163 solution onto the film and spincoating after 5 seconds. The conventional method results in 3D/LP

164 film with incomplete film formation with pin holes whereas the SPD Strategy results in film with  
165 homogeneous LP coverage. Scale bar is 1  $\mu\text{m}$ .

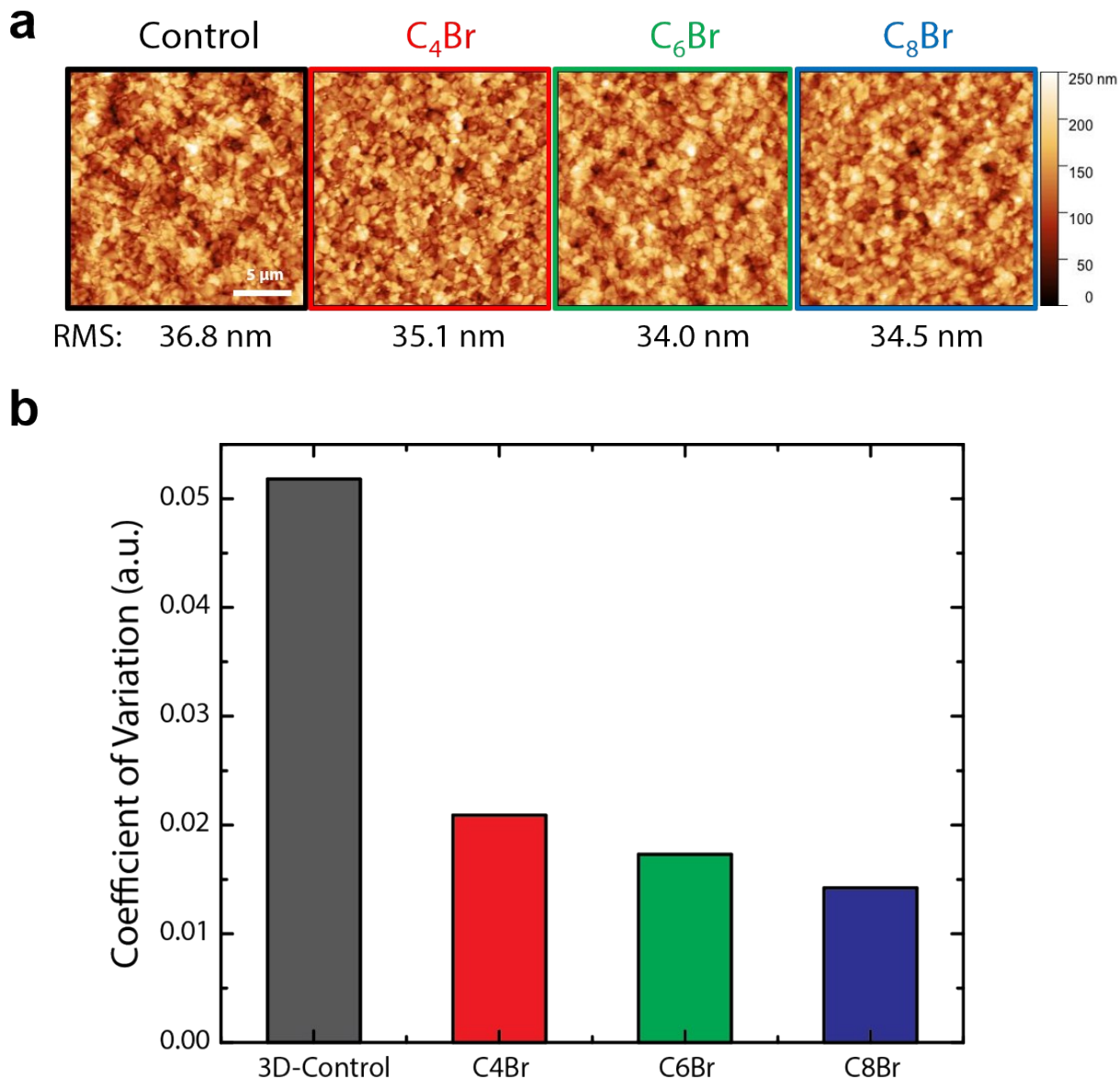
166



167

168 **Fig S5 a,** The XRD<sup>2</sup> shows the main LP peak shifting to lower angles with increasing alkyl chain  
 169 length. **b,** GIXRD pattern at various incident angle ( $\omega$ ) on the 3D perovskite and 3D/LPs with  
 170 different alkyl chain length.

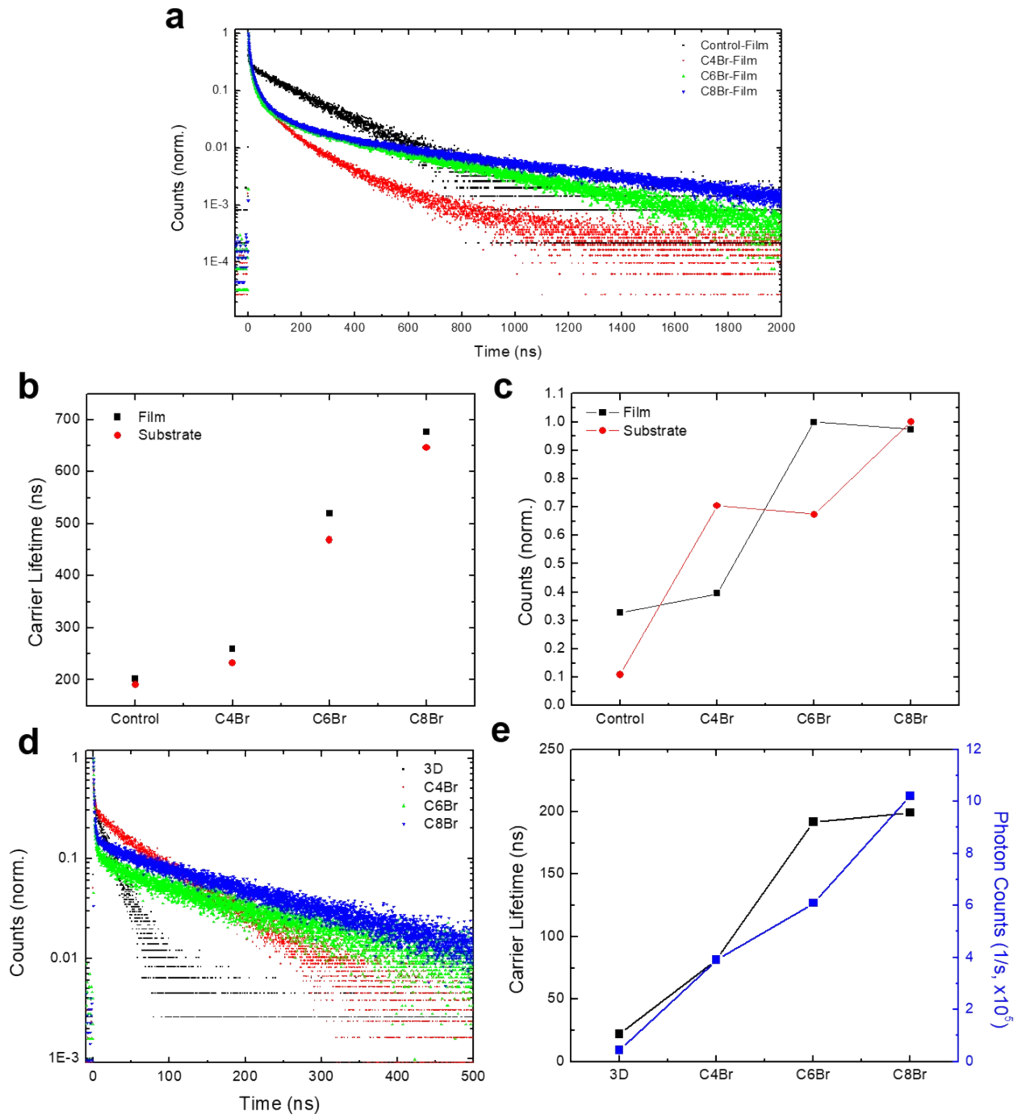
171



172

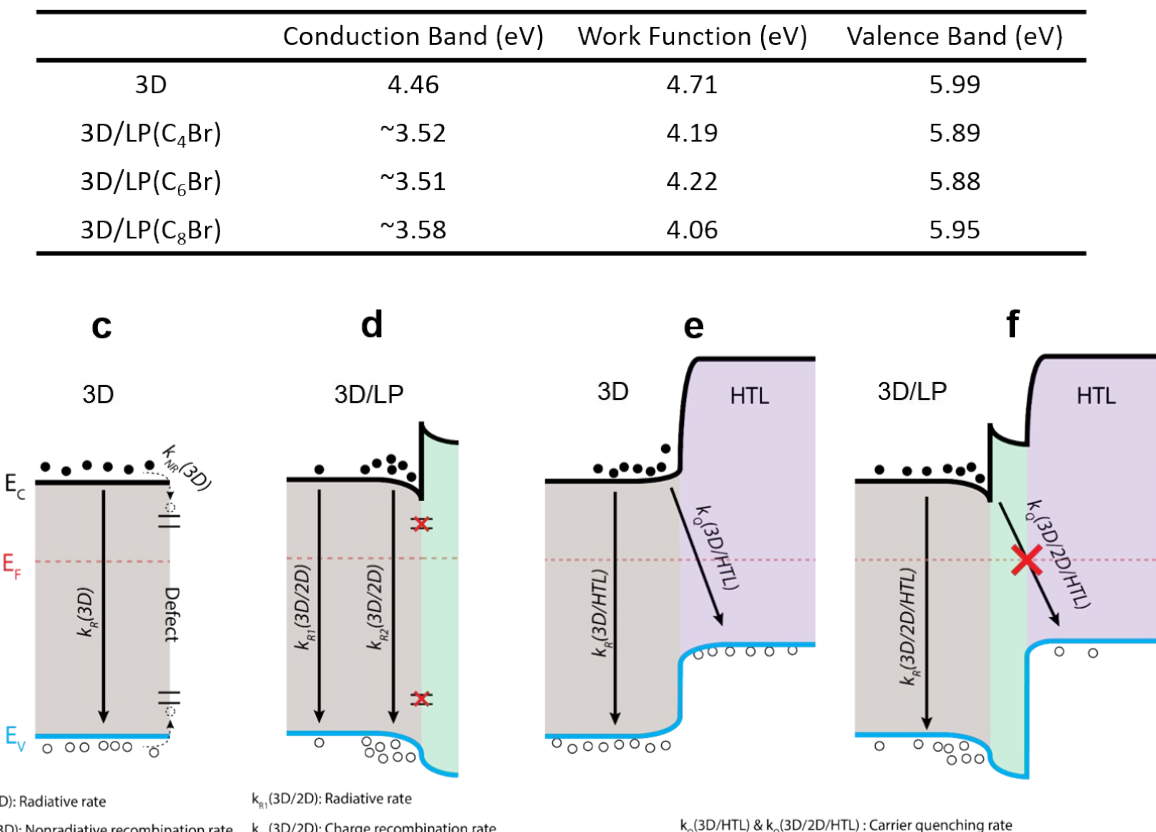
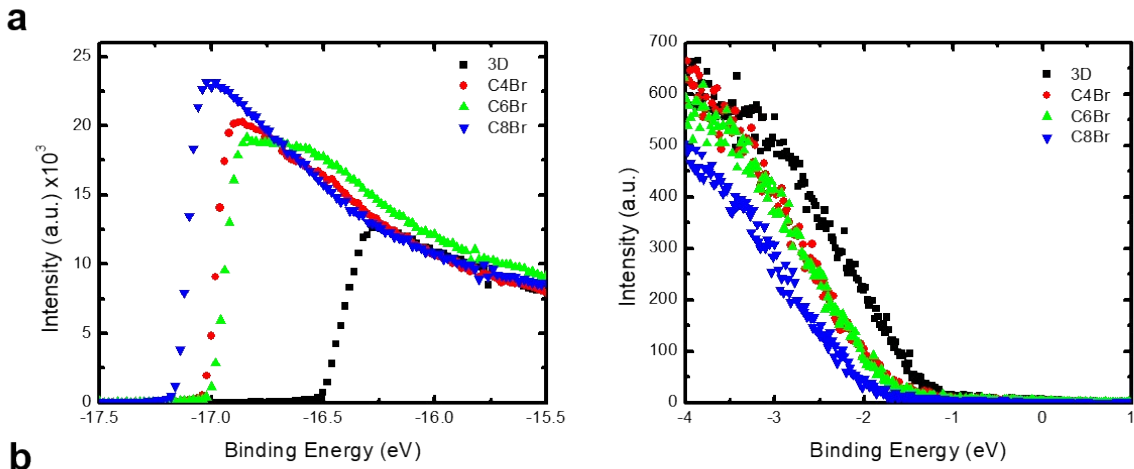
173 **Fig S6 a**, AFM images of 3D (Control) and 3D/LP ( $C_4\text{Br}$ ,  $C_6\text{Br}$ ,  $C_8\text{Br}$ ) perovskites and their  
 174 surface roughness shown in RMS value. Surface roughness decreases upon LP treatment. **b**,  
 175 Coefficient of variation, defined as the standard deviation of the CPD intensity normalized to the  
 176 average CPD intensity, calculated from KPFM images in Figure 2c.

177



178

179 **Fig S7 a,** TRPL traces of 3D and 3D/LPs on quartz substrates. “Film” indicates that the sample  
 180 is excited from the perovskite film side. **b,** Carrier lifetimes extracted by fitting the long  
 181 component of the lifetime traces (**a** above as well as from Figure 2**d**). “Substrate” indicates that  
 182 the sample is excited through the quartz substrate (in Figure 2**d**). **c,** Normalized integrated  
 183 photon counts from the TRPL measurements. **d,** TRPL of 3D and 3D/LP samples with Spiro-  
 184 OMeTAD as the hole transport layer, excited from the perovskite film side. **e,** Extracted carrier  
 185 lifetimes and integrated photon counts (from **d**).



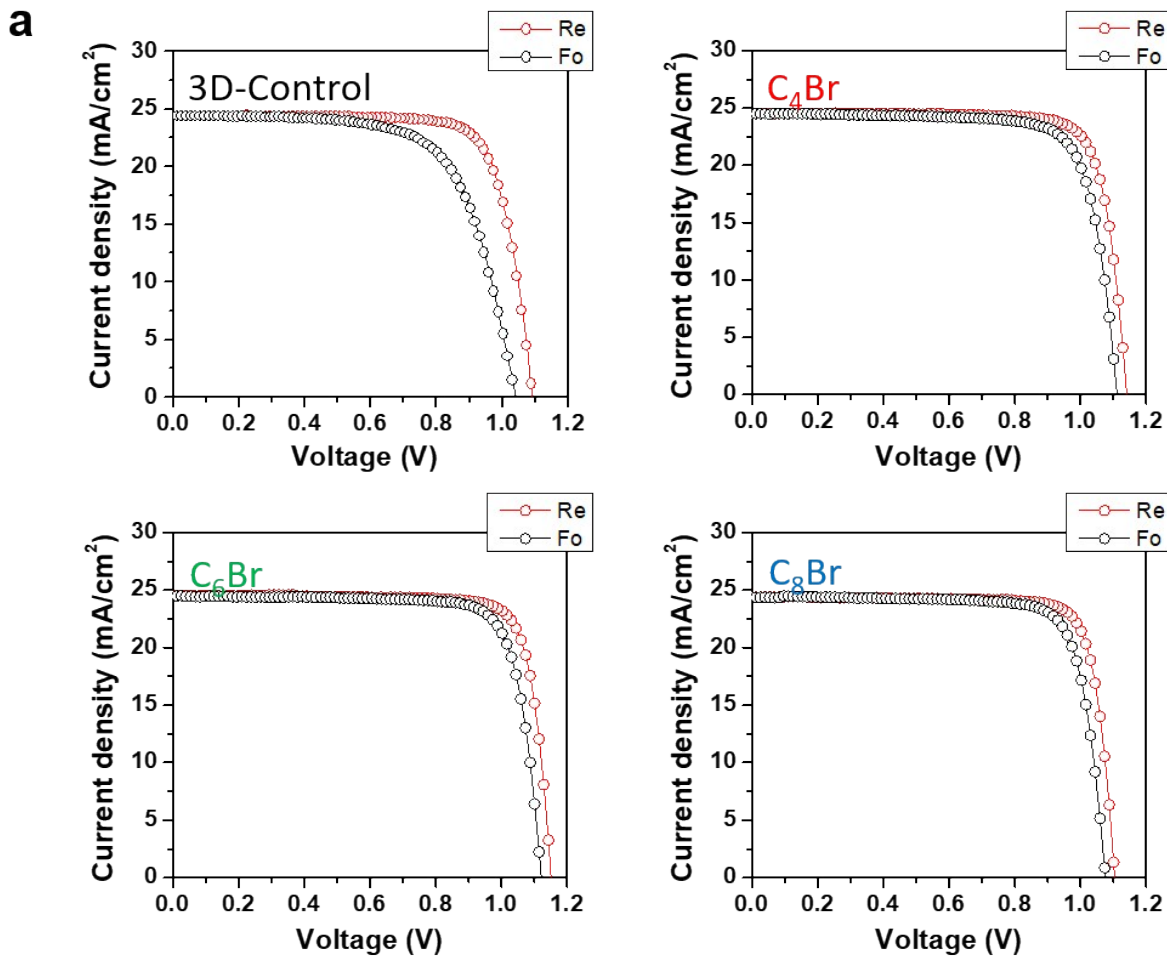
187 **Fig S8 a**, UPS spectra of 3D and three different 3D/LP substrates. **b**, Summary of energy levels  
 188 determined from UPS measurements. Bandgaps of 1.53 eV and 2.37 eV were used to determine  
 189 the conduction band of 3D and 3D/LPs, respectively. The bandgap for in-situ synthesized LP is  
 190 approximated by measuring the UVVis of a LP that is synthesized separately and not using the

191 3D perovskite as the template. **c-f**, Energy band diagrams of various perovskite layers  
192 determined from UPS and TRPL measurements. CB, WF, and VB correspond to conduction  
193 band, work function, and valence band, respectively. Energy band diagram of 3D control (**c**) and  
194 3D/LP (**d**), showing the passivation of surface defects with LP treatment. Energy band diagram  
195 of 3D control (**e**) and 3D/LP (**f**) with the addition of the hole transport layer (HTL).  
  
196 The band diagrams depicted in Extended Data Figure 8**c-f** to provide an explanation of the  
197 observed kinetics in the TRPL traces and the observed increased device performance.  
  
198 The 3D-control structure (Extended Data Figure 8**c**) depicts the band diagram and the observed  
199 recombination pathways based on TRPL measurements. The observed radiative rate,  $k_R(3D)$ , is  
200 faster than the known intrinsic carrier lifetime in 3D perovskite thin films, likely due to the  
201 presence of non-radiative recombination pathways,  $k_{NR}(3D)$ , associated with the surface. When a  
202 LP layer is deposited on the 3D perovskite (Extended Data Figure 8**d**), TRPL measurements  
203 observed with excitation from the 3D perovskite side show an increase in carrier lifetimes,  
204  $k_{R1}(3D/LP)$ , compared to the 3D control perovskite. On the other hand, the lifetime trace shows a  
205 relatively fast component,  $k_{R2}(3D/LP)$ , when the 3D/LP is excited from the LP side, in addition  
206 to the long component (Extended Data Figure 7**a**). This behavior of different lifetime profiles  
207 depending on the excitation side is not observed in the 3D control perovskite where the lifetime  
208 traces are almost identical for both film and substrate excitation. We identify the LP interlayer as  
209 a passivating layer that minimizes surface/interface trap states that otherwise would serve as non-  
210 radiative recombination centers. The additional passivation results in an increase in carrier  
211 lifetimes and the increase in detected photons. Furthermore, we hypothesize that the fast  
212 radiative component,  $k_{R2}(3D/LP)$ , is due to a carrier buildup at the 3D/LP interface from band  
213 bending, which is supported by the UPS results. This carrier accumulation can contribute to the

214 increase of  $V_{OC}$  of 3D/LP PSCs, in addition to the increase in the built-in potential due to the  
215 higher work function of 3D/LP.

216 Our hypothesis on the role of LPs on the 3D/LP structure is further supported by TRPL  
217 measurement with the addition of hole transport layers (HTL), specifically Spiro-OMeTAD.  
218 Extended Data Figure 8e-f shows the band diagram of 3D/HTL and the 3D/LP/HTL structure  
219 and Extended Data Figure 7d-e shows the corresponding lifetime traces, carrier lifetime, and  
220 photon counts. The 3D/HTL structure shows significantly faster lifetime traces when compared  
221 to pristine 3D perovskites, due to quenching of one of the carrier (hole) into the HTL. On the  
222 other hand, a longer lifetime is observed for the 3D/LP/HTL structure compared to 3D/HTL. The  
223 limited quenching effect can be explained by the reduced recombination between the electron in  
224 the perovskite layer and the hole in the HTL due to the spatial separation and the energy barrier  
225 provided by the wide bandgap LP.

226 In total, the LP interlayer passivates the 3D perovskite surface traps and minimizes nonradiative  
227 recombination pathways, while providing a spatial separation and an energy barrier to minimize  
228 carrier quenching associated with the 3D perovskite/HTL interface. In eliminating intra-band gap  
229 states and removing nonradiative recombination pathways, the LP interlayer provides an ideal  
230 interface for low  $V_{OC}$  loss and improved PCE.

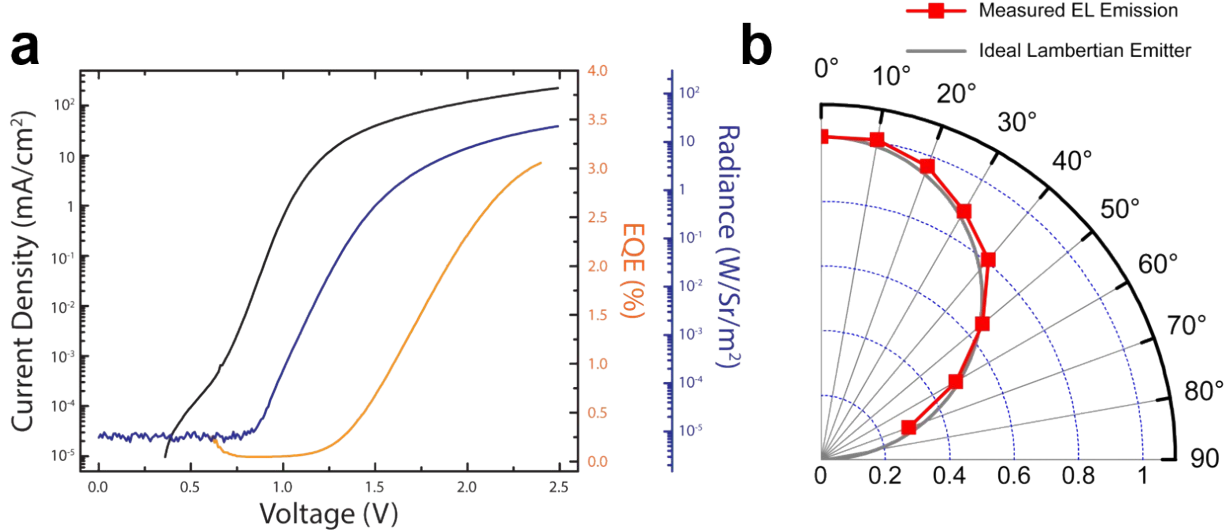


**b**

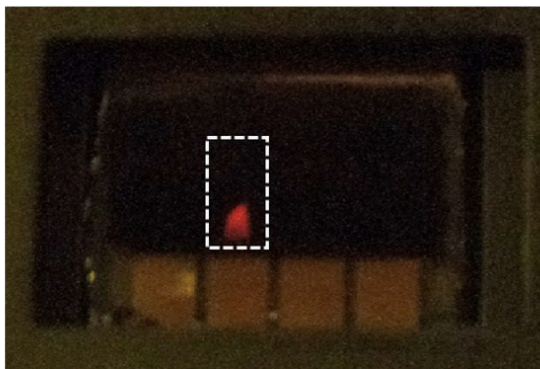
	$V_{OC}$ (V)	$J_{SC}$ ( $\text{mA}/\text{cm}^2$ )	FF (%)	PCE (%)
3D	$1.10 \pm 0.01$	$24.0 \pm 0.4$	$78.5 \pm 1.0$	$20.7 \pm 0.4$ (21.7)
$C_4\text{Br}$	$1.14 \pm 0.01$	$24.0 \pm 0.5$	$79.9 \pm 1.1$	$22.0 \pm 0.6$ (23.2)
$C_6\text{Br}$	$1.15 \pm 0.01$	$24.2 \pm 0.4$	$80.3 \pm 1.1$	$22.4 \pm 0.4$ (23.2)
$C_8\text{Br}$	$1.15 \pm 0.01$	$24.2 \pm 0.3$	$79.8 \pm 1.2$	$22.1 \pm 0.4$ (23.1)

231

232 **Fig S9 a**,  $J$ - $V$  curves of 3D and 3D/LP representative PSCs showing reduced hysteresis for LP  
 233 treated PSCs. “Re” is the reverse scan the “Fo” is the forward scan. **b**, PCE average and standard  
 234 deviation for 3D and 3D/LP PSCs measured over 20 devices. The PCE values in parentheses  
 235 represent the result for the best-performing cells.

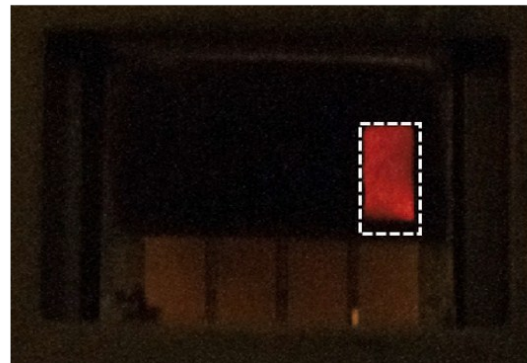


**C Conventional Method (IPA)**



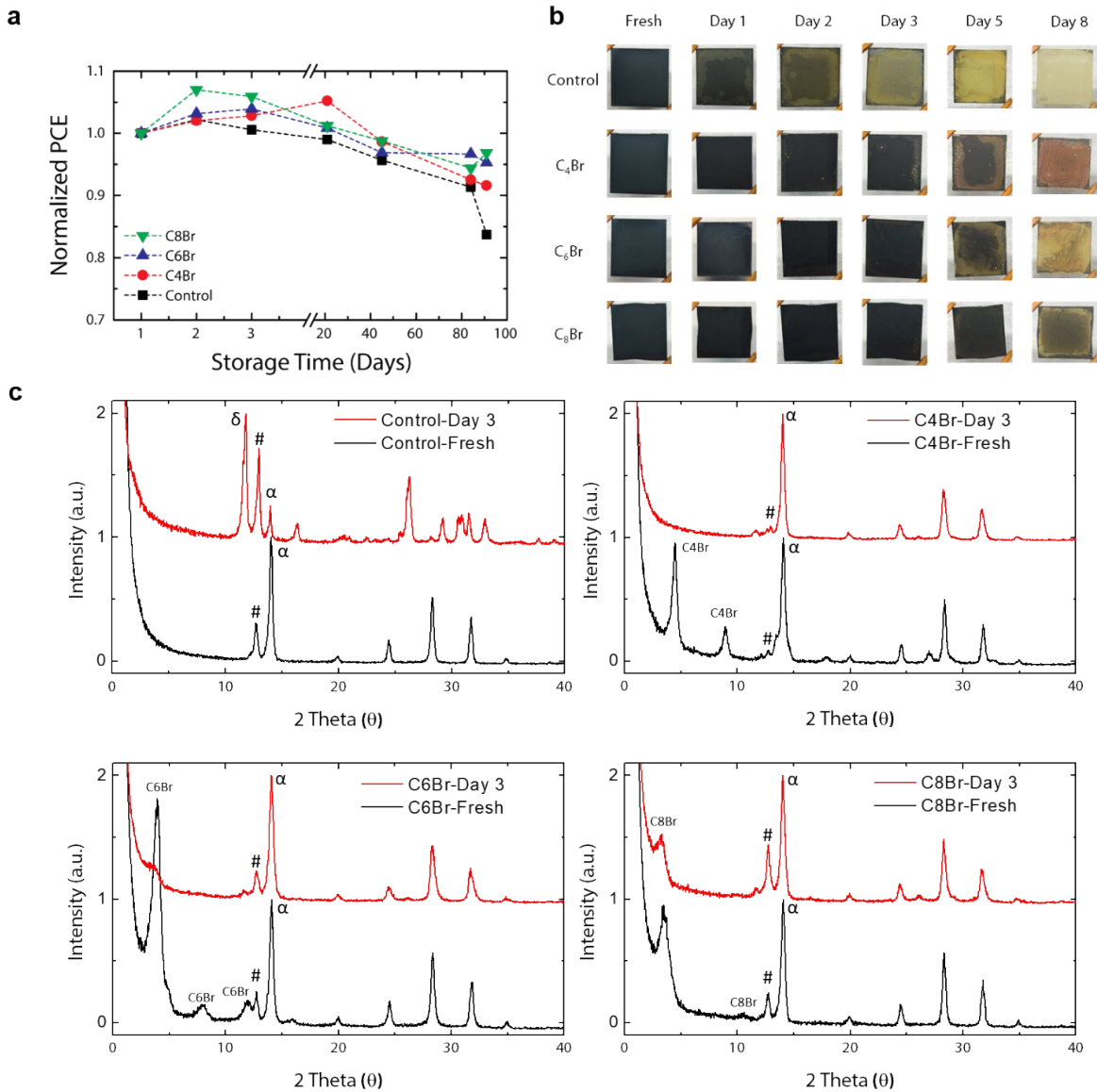
236

**SPD strategy (CF)**



237 **Fig S10 a**, Plot of current density, EQE, and radiance as a function of voltage from the 3D  
 238 control PSC. The device shows a max EQE of 3.0%. **b**, EL emission profile of a PSC showing an  
 239 emission profile that resembles an ideal Lambertian emitter. **c**, Photograph of 3D/LP PSC  
 240 operating as an LED. PSCs fabricated using the conventional method shows non-uniform EL  
 241 emission from the active area (white dotted line), whereas devices fabricated using our newly  
 242 developed STD strategy shows uniform and complete EL emission from the active area.

243

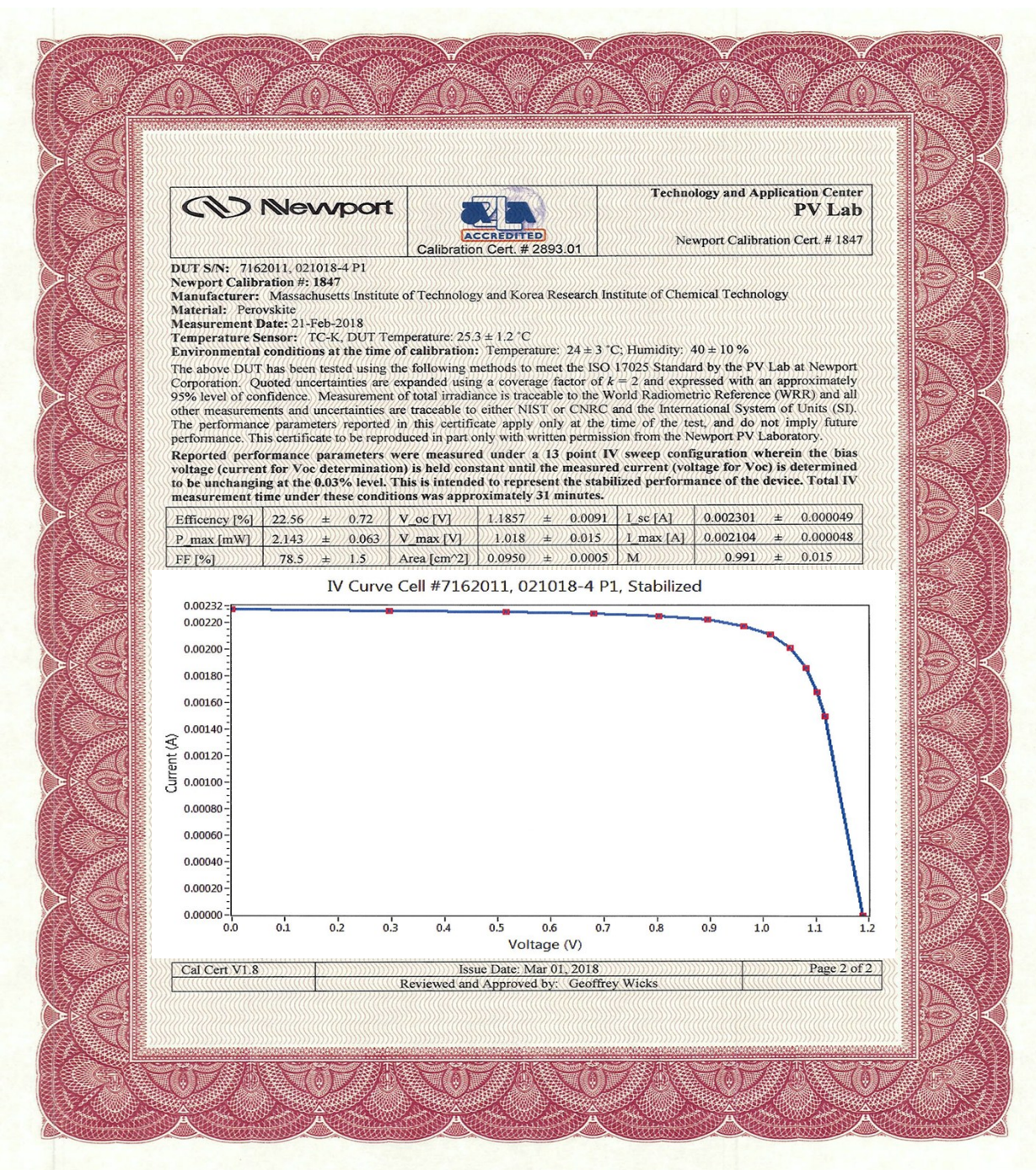


244

245 **Fig S11 a**, Normalized PCE as a function of storage time for 3D and 3D/LP PSCs. The devices  
 246 were stored in dark and dry conditions between measurements. **b**, Photographs of 3D and 3D/LP  
 247 films on glass substrates stored in a humidity chamber (~90% RH) at room temperature as a  
 248 function of storage time. The bleaching indicates decomposition of the 3D perovskite. The  
 249 3D/LP films showed higher resistance to moisture than the 3D control. An increase in alkyl chain  
 250 provides additional resistance. **c**, XRD pattern of 3D and 3D/LP films on glass stored in the  
 251 humidity chamber. The 3D control showed severe decomposition of the perovskite into  $\text{PbI}_2$

252 (marked with #) and δ-phase perovskite on day 3, whereas 3D/LPs showed no sign of significant  
253 δ-phase formation.

254



255

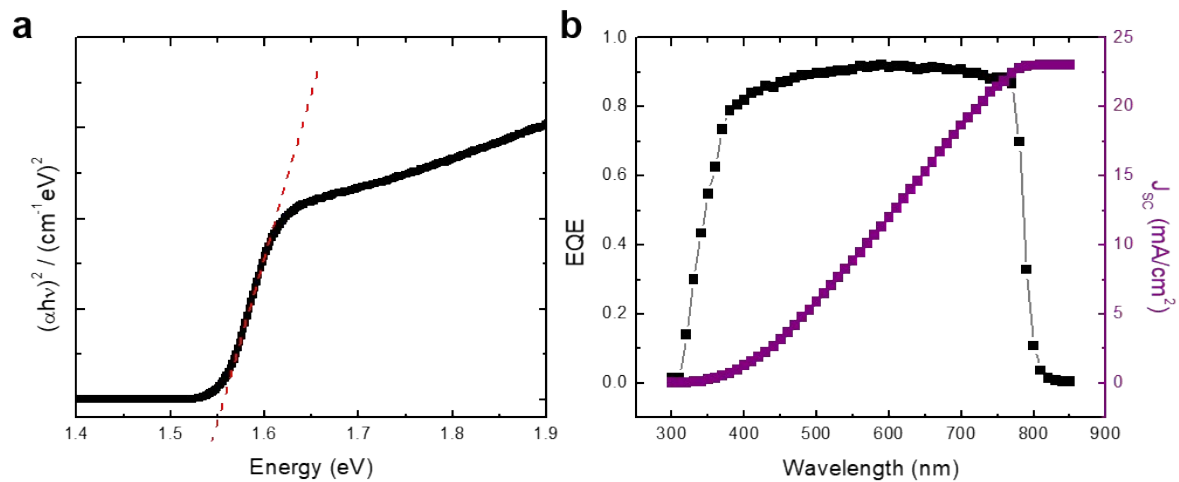
256 Fig S12 Certification of 3D/LP PSC with stabilized J-V curve tested at an independent and  
257 accredited PV testing lab (Newport).

258

259

260

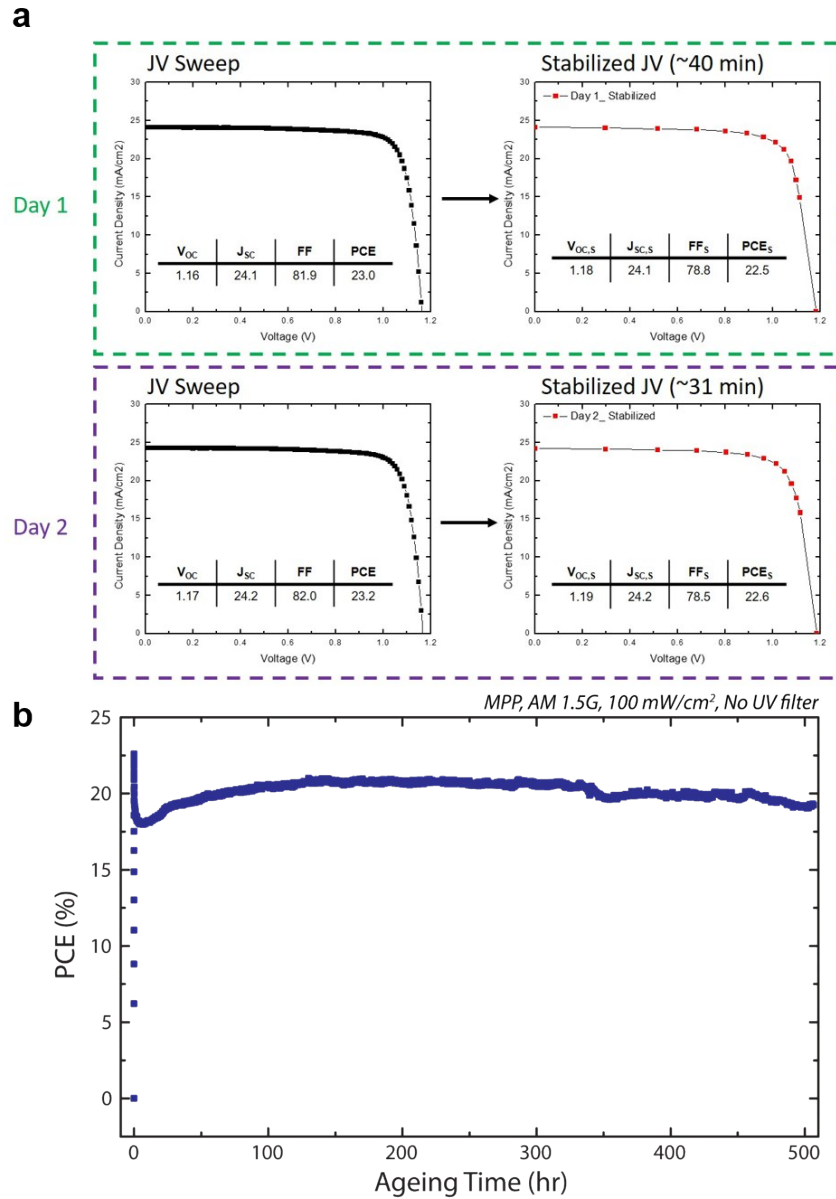
261



262

263 **Fig S13 a,b**, Tauc plot from UV-Vis absorption spectrum (**a**) and external quantum efficiency  
264 (EQE) plot (**b**) used to determine the bandgap. Bandgap determined from tangent line from UV-  
265 Vis tauc plot is ~1.56 eV and from the EQE plot is ~1.55 eV. The bandgap determined from  
266 EQE onset is ~1.53 eV. The integrated current density determined from the EQE spectrum is  
267 also shown in **b**.

268



269

270 **Fig S14 a**, 3D/LP PSC device results on the same pad on two consecutive days (measurement at  
271 Newport). The 3D/LP PSC shows almost identical results even after extensive stabilization  
272 measurement (~40 min on day 1 and ~31 min on day 2) demonstrating remarkable operational  
273 stability. **b**, The MPP was measured under full solar illumination (AM 1.5G, 100 mW/cm<sup>2</sup>)  
274 without a UV-filter. The PSC shows an initial PCE of 22.6% and maintained 85% of its  
275 efficiency after 500 hrs. The device is encapsulated and measured in ambient condition.